



## Impacts of the Tibetan Plateau on aridity change over the Northern Hemisphere



Zhaokui Gao<sup>a</sup>, Xiaodan Guan<sup>a,\*</sup>, Bian He<sup>b</sup>, Long Zhao<sup>c</sup>, Yongkun Xie<sup>a</sup>, Yongli He<sup>a</sup>, Fei Ji<sup>a</sup>

<sup>a</sup> Collaborative Innovation Center for Western Ecological Safety, College of Atmospheric Sciences, Lanzhou University, Lanzhou 730000, China

<sup>b</sup> State Key Laboratory of Numerical Modeling for Atmospheric Sciences and Geophysical Fluid Dynamics (LASG), Institute of Atmospheric Physics, Chinese Academy of Sciences, Beijing 100029, China

<sup>c</sup> School of Geographical Sciences, Southwest University, Chongqing 400715, China

### ARTICLE INFO

#### Keywords:

Tibetan Plateau  
Aridity index  
Multi-decadal variability  
Dynamic effect  
Thermal effect

### ABSTRACT

Aridity change in the Northern Hemisphere (NH) is a vital topic in exploring climate change. The Tibetan Plateau (TP) is essential for its role in climate variability over the NH. We applied the ensemble empirical mode decomposition (EEMD) to the aridity index (AI) from 20°–60°N in this study. The EEMD method extracts a set of intrinsic mode functions (IMFs) with various timescales. Results from our analysis reveal that the multi-decadal oscillation of AI makes 35% contribution to the variability of the AI. And the multi-decadal oscillation of the TP thermal forcing makes 18.15% contribution to the multi-decadal variability of the AI, which is often ignored in previous studies. The dynamic and thermal effects of the TP also affect the AI change, which illustrates a mode of meridional difference around 40°N, with wetting in the north and drying in the south. Meanwhile, the dynamic effects of the TP lead to latitudinal difference north of 40°N in Asia, with drying Northeast Asia. Such meridional and latitudinal differences over South Asia, Southeast Asia and southern China are controlled by a high-pressure system from 850 hPa up to 500 hPa, which results in an increase of sinking motion from 20°–40°N with obvious continuous drying effect.

### 1. Introduction

The Tibetan Plateau (TP) is located in subtropical Asia, with an average elevation of over 4000 m and complex landscape (Chen et al., 2021; Wen et al., 2021). As the largest plateau on Earth, it covers 2.5 million square kilometers, approximately 25% of China's land area (Jane, 2008; Xu et al., 2008b). As the TP stores a large amount of terrestrial water in its lakes, rivers, snow, and glaciers, it is named the global atmospheric "water tower" (Xu et al., 2014; Qiao et al., 1984). In summer, the atmospheric moisture over the TP is higher than that over its surrounding areas (Xu et al., 2008a; He et al., 2021); and the moisture can be transported from the surface layer to the stratosphere, affecting the global troposphere-stratosphere moisture budget (Chen et al., 2012). The land-atmosphere coupling of the TP has profound implications for global climate due to its location, altitude, area, steep slopes, and abundant water resources (Ma et al., 2008; Liu et al., 2020a). In particular, the dynamic and thermal forcing of the TP may play a critical role in regional climate (Ma et al., 2017a; Wu et al., 2020), and further influence the aridity in the Northern Hemisphere (NH) (Chen et al.,

2021; Sun and Liu, 2021).

The uplift of the TP has had a profound and sustained impact on the current global climate (Liu and Dong, 2013). It increases the thermal difference between land and ocean, becoming a heat source in summer (Ye and Wu, 1998; You et al., 2020). The thermal forcing over the TP generates a monsoonal meridional circulation over South Asia, and sets up favorable large-scale ascent condition for the development of the Asian summer monsoon (ASM) (Yanai et al., 1992; Ma and Ma, 2016; Ma et al., 2017b). The division of the westerlies into southern and northern branches by the dynamic effect of the TP leads to the blockage of the ASM and eventually to the aridity of East Asian inland. It can also increase the aridity of inner Asia by blocking water vapor from the nearby ocean and inducing sinking airflow (Ye and Gao, 1979; Sun and Liu, 2021).

Changes in thermal forcing over the TP affect atmospheric circulations, contribute significantly to precipitation over downstream regions, and further impact the aridity over the NH (Zhang et al., 2006; Ma et al., 2017b). TP heating leads to the meridional shift of the subtropical and mid-latitude westerly jet (SWJ), and an extension of the South Asian

\* Corresponding author.

E-mail address: [guanxd@lzu.edu.cn](mailto:guanxd@lzu.edu.cn) (X. Guan).

high (Liu et al., 2020b). The atmospheric circulations, especially the ASM and westerly jet, play important roles in transporting water vapor and clouds from the TP (Zhang et al., 2006). Simultaneously, the TP acts as a channel for driving water vapor, clouds and aerosols from the surface layer to the stratosphere (Zhang et al., 2006; Xu et al., 2018).

Aridity is commonly defined by the ratio of precipitation (P) to potential evapotranspiration (PET) (Middleton and Thomas, 1997). Increased aridity leads to severe soil moisture deficits, decreases in carbon uptake, and an expansion of global drylands, altering landscapes, ecosystems, and the conditions people live in (Lickley and Solomon, 2018). Regions with  $P/PET < 0.65$  are defined as drylands, which are sensitive and vulnerable to climate change (Prvlie, 2016). Large areas of drylands are located in the mid-latitudes of the NH, which are inhabited by large population (Prvlie, 2016), with the highest population density distributed in South and East Asia, North Africa, and the Middle East (Zhang and Zhou, 2015).

Previous studies attributed the decadal variation of aridity to dynamic oscillations, such as the Atlantic Multi-decadal Oscillation (AMO), Pacific Decadal Oscillation (PDO), Arctic Oscillation (AO), and El Niño-Southern Oscillation (ENSO) (Wang et al., 2007; Chang et al., 2004; Wang et al., 2014; Guan et al., 2017; Li et al., 2019). The effects of the apparent heat source  $Q_1$  of the TP on aridity changes over the NH received less attention. In this study, we quantified the effects of the  $Q_1$  on aridity change in the NH, and explored the impacts from the uplifted TP on aridity in the NH. Terrain sensitivity experiments from the Global Monsoons Model Intercomparison Project (GMMIP) were used to investigate the sustained impact from the TP on aridity (Zhou et al., 2019; He et al., 2020). We first analyzed the effect from the TP on the aridity change on multi-decadal time scales, and explored the dynamic and thermal effects from the TP on aridity with three sensitivity experiments. This paper is organized as follows. In Section 2, we describe the data and analysis methods. The analysis of results is in Section 3. Conclusions and discussion are presented in Section 4.

## 2. Material and methods

### 2.1. Material

#### 2.1.1. Aridity Index

The aridity index (AI) is denoted as follows,

$$AI = \frac{P}{PET} \quad (1)$$

we calculate the AI as in Huang et al. (2020). The precipitation data we use is PRECipitation REConstruction over Land (PREC/L) dataset (Chen et al., 2002) developed at the Climatic Prediction Center (CPC) of National Oceanic and Atmospheric Administration (NOAA), which is on  $0.5^\circ$ , covering the period from 1948 to the present. The PET data is from the Climatic Research Unit (CRU) TS 4.06 dataset (Harris et al., 2014), which covers the period of 1901–2021 with a resolution of  $0.5^\circ$ . The observed precipitation and PET data are provided by Feng and Fu (2013).

We calculated the AI using Eq. (1) and monthly Chinese Academy of Sciences (CAS) Flexible Global Ocean-Atmosphere-Land System (FGOALS-f3-L) model outputs. Using near-surface air temperature (TAS), 2-m wind speed ( $|u|$ ), relative humidity (RH), heat flux into ground ( $G$ ), and the net downward broadband radiation ( $R_n$ ), we calculated simulated PET using the Penman-Monteith algorithm (Penman, 1948; Monteith, 1981; Allen et al., 1998), as shown below,

$$PET = \frac{(R_n - G)\Delta(TAS) + \rho_a C_p e^*(TAS)(1 - RH)C_H |u|}{\Delta(TAS) + \gamma(1 + r_s C_H |u|)} / L_v \quad (2)$$

where  $\Delta$  is the slope of the Clausius-Clapeyron curve,  $\rho_a$  is air density,  $C_p$  is the specific heat of air,  $e^*(TAS)$  is the saturated water vapor pressure at given TAS,  $C_H \approx 4.8 \times 10^{-3}$  is the bulk transfer coefficient,  $r_s \approx 70\text{s/m}$

is the bulk stomatal resistance,  $L_v$  is the latent heat of water vaporization, and  $\gamma$  is the psychrometric constant.  $(R_n - G)$  in climate model outputs could be replaced by the sum of sensible heat (SH) and latent heat (LH). (Allen et al., 1998; Fu and Feng, 2014; Scheff and Frierson, 2014; Wei et al., 2019).

The CAS-FGOALS-f3-L modeling team completed Phase 6 of the Coupled Model Inter-comparison Project (CMIP6) Global Monsoons Model Inter-comparison Project (GMMIP). GMMIP Tier-1 historical simulation (hist) and GMMIP Tier-3 simulations are used in this paper. Specifically, the Tier-3 simulations are one orographic perturbation experiment that removes the topography of the Tibetan-Iranian Plateau (TIP) at altitude above 500 m (referred to as NTIP), and one thermal perturbation experiment that removes the sensible surface heating over the TIP and surrounding regions at altitude above 500 m (referred to as NTIP-nosh). The outputs cover the period 1979 to 2014 with a resolution of  $1.0^\circ \times 1.25^\circ$  (latitude  $\times$  longitude). The variant label of the outputs is r1i1p1f1 (Zhou et al., 2019; He et al., 2020).

### 2.1.2. Apparent Heat Source $Q_1$

Following previous investigations (Yanai et al., 1973; Yanai and Tomita, 1998), apparent heat source  $Q_1$  can be calculated using

$$Q_1 = c_p \left( \frac{p}{p_0} \right)^\kappa \left( \frac{\partial \theta}{\partial t} + V \cdot \nabla \theta + \omega \frac{\partial \theta}{\partial p} \right) \quad (3)$$

where  $\theta$  is potential temperature (units: K),  $V$  is horizontal wind (units: m/s),  $\omega$  is the vertical velocity on isobaric surface (units: Pa/s),  $p$  is pressure (units: Pa),  $p_0 = 1000$  hPa, and  $\kappa = \frac{R}{c_p}$  (units: J/(kg)).  $R$  and  $c_p$  are the gas constant and specific heat at constant pressure of dry air, respectively.  $\nabla$  is the isobaric gradient operator.

The vertically integrated apparent heat source  $Q_1$  was obtained by integrating Eq. (3), where  $p_s$  is surface pressure level. As the average elevation of the TP is approximately 4000 m, the minimum of  $p_s$  used in this study is 600 hPa; thus,

$$Q_1 = \frac{1}{g} \int_{100}^{p_s} Q_1 dp \quad (4)$$

Note that positive (negative)  $Q_1$  indicates a net heat gain (loss). We calculated  $Q_1$  according to the method mentioned in Liu et al. (2021); and we kept the climatology of  $Q_1$  consistent with that provided by Liu et al. (2021).

### 2.1.3. Oscillation Indices

Four climate indices of the Nino3.4, PDO, AMO, and AO, are taken from the KNMI Climate Explorer. The Nino3.4 index is the sea-surface temperatures (SST) anomaly averaged over  $(170^\circ\text{--}120^\circ\text{W}, 5^\circ\text{S}\text{--}5^\circ\text{N})$  (Trenberth, 1997). The PDO index is defined as the leading Empirical Orthogonal Function (EOF) pattern and associated time series of monthly SST over  $(110^\circ\text{E}\text{--}100^\circ\text{W}, 20^\circ\text{--}70^\circ\text{N})$ , with global mean SST series removed (Mantua et al., 1997). The AMO index is defined as the SST averaged over  $(0^\circ\text{--}80^\circ\text{W}, 0^\circ\text{--}70^\circ\text{N})$ , by subtracting mean SST over  $60^\circ\text{S}\text{--}60^\circ\text{N}$  (Enfield et al., 2001; Trenberth and Shea, 2006). The AO index is defined as the standardized leading principal component time series of monthly mean NH sea-level pressure for all months of the year (Thompson and Wallace, 1998). Note that the four indices of the Nino3.4, PDO, AMO, and AO cover the period from 1950 to 2021, to coincide with the period of the  $Q_1$  data.

## 2.2. Methods

### 2.2.1. Wavelet Decomposition

Wavelet analysis can describe non-stationary signals whose frequencies vary with time. Readers may refer to Torrence and Compo (1998) for a detailed introduction to wavelet analysis. A continuous wavelet analysis is used to identify the primary frequency of the AI, and to explore the change of this frequency over time. The analysis

decomposes a signal into a series of wavelets obtained by scaling and shifting the basic functions. The wavelet basis function is shown in Eq. (5). The wavelet transform has two parameters: scale parameter  $a$  and translation parameter  $\tau$ .  $a$  corresponds to frequency, and  $\tau$  corresponds to time:

$$\Psi_{a,b}(t) = \frac{1}{\sqrt{a}} \Psi\left(\frac{t-b}{a}\right) \quad (5)$$

The continuous wavelet transform is performed on signal  $X(t)$  to generate the wavelet spectrum, which is defined as follows,

$$X(a, b) = \int_{-\infty}^{+\infty} X(t) \frac{1}{\sqrt{a}} \Psi\left(\frac{t-b}{a}\right) dt \quad (6)$$

The software of wavelet decomposition in IDL is available at <https://paos.colorado.edu/research/wavelets/>.

### 2.2.2. Ensemble Empirical Mode Decomposition Method

The ensemble empirical mode decomposition (EEMD) method was adopted in this study to decompose the time series of the AI. This method is an adaptive and noise-assisted data analysis method, suitable for non-stationary and nonlinear signal detection. Original climate signals can be decomposed into different oscillatory components with different time scales (intrinsic mode function [IMF]) and trends. The steps can be briefly described as follows (Huang et al., 1998; Wu and Huang, 2009).

- (1) Add a white noise time series to the targeted data series  $x(t)$ ;
- (2.1) Set  $x_1(t) = x(t)$  and identify all the maxima and minima of  $x_1(t)$ , connect all maxima points to obtain the upper envelope  $e_u(t)$  and connect all minima points to obtain the lower envelope  $e_l(t)$  with cubic splines, respectively;

(2.2) According to the given criteria, calculate the mean  $m(t)$  between the two envelopes;

$$m(t) = [e_u(t) + e_l(t)]/2 \quad (7)$$

Then, determine whether  $m(t)$  is close to zero (equivalent to the symmetric of the upper and lower envelopes about the zero line) at any location;

(2.3) If yes, stop the screening process; if not, set  $x_1(t) = x(t) - m(t)$  and repeat steps 2.1 and 2.2;

(2.4) After this, the original time series  $x(t)$  can be expressed as the first intrinsic mode function (IMF) and a remainder. If the remainder still contains oscillatory components, we again repeat steps 2.1 and 2.2, but set  $x_1(t)$  as the remainder.

Therefore, each time series can be expressed as the sum of different IMFs and a remainder, which can be expressed as:

$$x(t) = \sum_{j=1}^n C_j(t) + R_n(t) \quad (8)$$

where  $n$  indicates the number of IMFs,  $C_j(t)$  indicates the  $j$ th IMF, and  $R_n(t)$  denotes the final remainder that is either monotonic or contains only one extreme.

(3) Repeat steps 1 and 2 again and again, but add different white noise time series each time and obtain the (ensemble) means for corresponding IMFs of the decompositions as the final result. According to Ji et al. (2014), noise added to the data has an amplitude that is 0.2 times the standard deviation of the raw data; and the ensemble number is 400. The EEMD codes are from Dr. Zhaohua Wu in MATLAB (Wu's website: <https://www.coaps.fsu.edu/zhaohua-wu>).

## 3. Results

### 3.1. Changes of Aridity

Regions with  $AI < 0.65$  are defined as drylands, which are further classified into four subtypes of hyperarid ( $AI < 0.05$ ), arid ( $0.05 < AI < 0.2$ ), semiarid ( $0.2 < AI < 0.5$ ), and dry subhumid ( $0.5 < AI < 0.65$ )

regions (Middleton and Thomas, 1997). The drylands of the world are mainly distributed in the mid and high latitudes of the NH. The drylands are mainly distributed in North Africa, the Iberian Peninsula, West Asia, central Asia, Northwest China, the Mongolian Plateau, and the western United States. The humid regions are mainly distributed in Europe, north of  $50^\circ\text{N}$ , South China, the southern foothills of the Himalayas, east of  $120^\circ\text{E}$ , and eastern North America. Fig. 1 shows apparent spatial heterogeneity, with latitudinal distribution in East Asia and longitudinal distribution in North America.

The time series of the AI shows an increasing trend from 1948 to 1983 (the first blue shading period in Fig. 2a). Then, the AI decreased significantly from the early-1980s to the early-2000s (the red shading period), followed by a significant increase to its highest point of 0.48 in 2020 (the second blue shading period). Li et al. (2019) noted that the AI showed significant differences before and after 1980, and it also changed significantly around the 2000s. The 11-year running mean of annual AI (red curve) shows that the AI has experienced evident multi-decadal variability with distinct downward and upward phases.

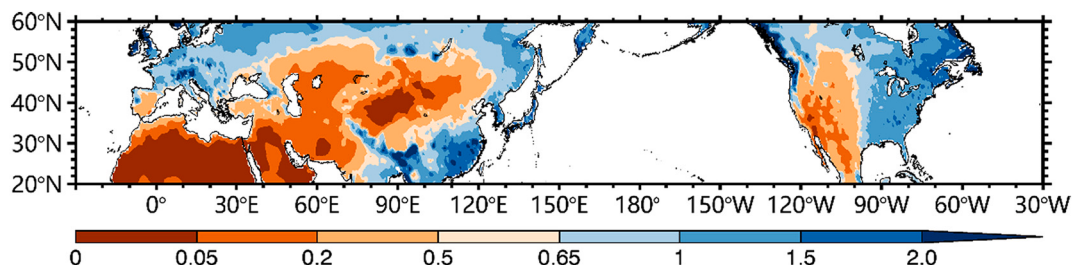
By applying the wavelet decomposition to the time series of AI anomalies over the NH from  $20^\circ$  to  $60^\circ\text{N}$ , we computed the wavelet power spectrum of the AI to examine its multi-decadal variation. The local spectrum of the AI is shown in Fig. 2b, and the global spectrum is in Fig. 2c. A continuous regions of 58–66-year cycle passed the 95% significance test during 1948–2021. Significant power can also be found at 11–14-year cycle, while only periods of 1948–1960 and 1980–2021 pass the significant test. The dominant period of the AI is 58–66-year from 1948 to 2021. There is also a 3.5-year period that passed the 95% significance test around 1990. After detrending the AI, the multi-decadal variability (58–66-year) is dominant in the global spectrum of the AI, with global power  $> 0.15$  and reaching its maximum of 0.65 around the 66-year cycle.

As the EEMD method can split the evolution of AI variability into long-term trend and oscillation components (Liu et al., 2021), we further applied the EEMD method to decompose the time series of AI anomaly in the NH from  $20^\circ$  to  $60^\circ\text{N}$ , which covers the period from 1948 to 2021. We obtained five IMF components (C1–C5) and a long-term trend (C6) (Fig. 3). The five IMF components reflect the variation characteristics from high to low frequency at different timescales. The oscillation cycles of C1 and C2 are about 3 and 7 years, respectively. The oscillation cycles of C3, C4, and C5 are about 13, 28, and 71 years, respectively, which are induced mainly by the internal climate variability (ICV) (Huang et al., 2017). The long-term trend is closely associated with radiative forcing (Luo et al., 2019).

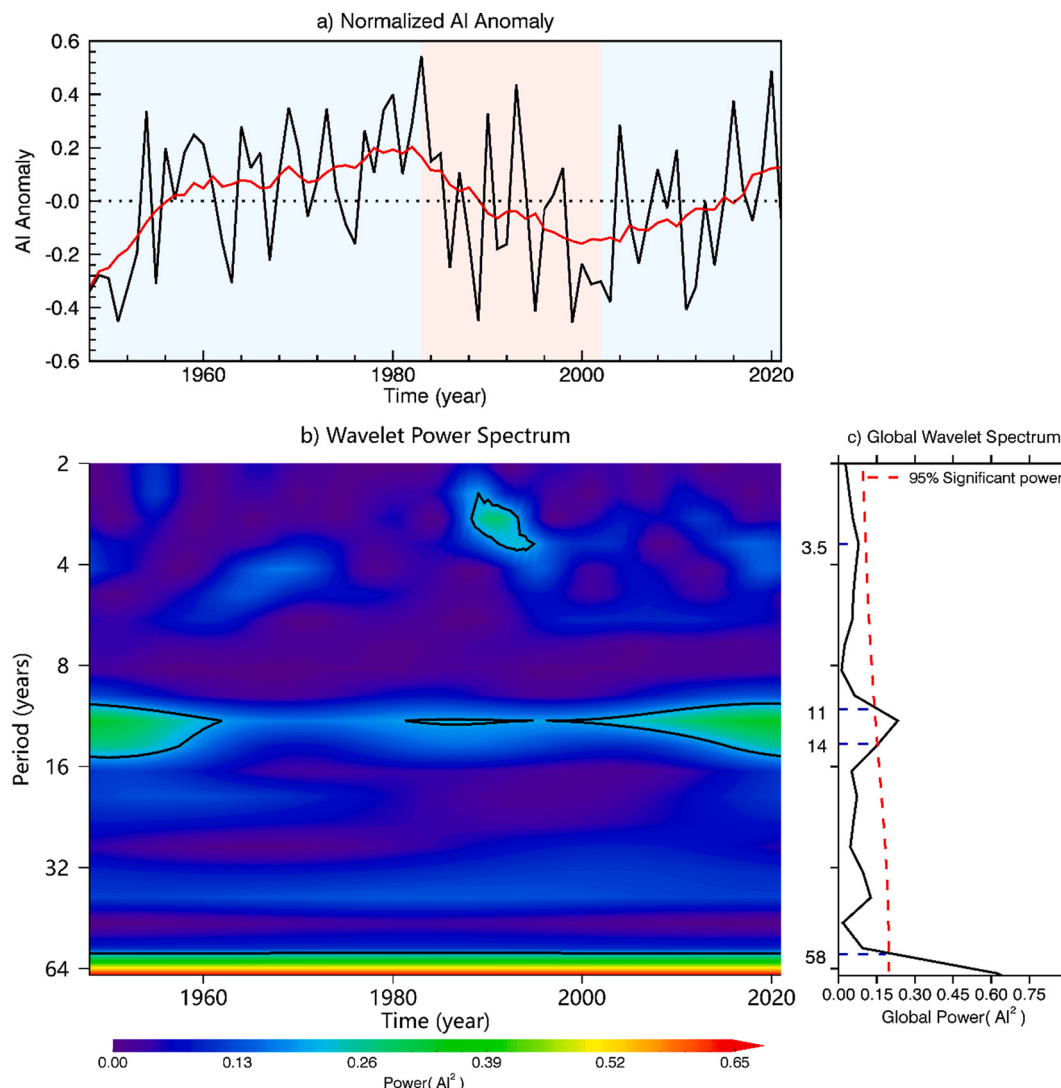
According to the IMF components with different oscillation cycles, we rebuilt the IAV, IDV, MDV, and the long-term trend of the AI anomalies from 1948 to 2021 in Fig. 4. IMFs C1 and C2 are at the interannual timescale, so their sum is called the interannual variability (IAV; black curve in Fig. 4). IMF C3 is named as the inter-decadal variability (IDV; yellow curve in Fig. 4). IMFs C4 and C5 are at the multi-decadal timescale, so their sum is named as multi-decadal variability (MDV; red curve in Fig. 4). The long-term trend is the residual (C6; blue dashed curve in Fig. 4). When the MDV is in an upward phase, it dominated the uptrend of the AI (wetting) from 1948 to 1960, 1970 to 1980 and from 2000 to 2021. When the MDV is in a downward phase, it dominated the downtrend of the AI (drying) from 1980 to the 2000s.

Table 1 shows contributions of the IAV, IDV and MDV components to the AI. The IAV and IDV components contribute 49% and 16% respectively. As the dominant component of the AI, the MDV contributes 35%. The contribution of the MDV makes the second most contribution to the variability of the AI. To explore the spatial variation of the AI at different timescales, we decomposed the temporal record of the AI in each location, and plotted the evolution of zonally averaged annual-mean anomalies, IAV, IDV, and MDV of the AI in Fig. 5.

In Fig. 5a, the zonal patterns of the annual-mean anomalies of the AI show significant differences prior to and after 2000. The AI in  $20^\circ$ – $60^\circ\text{N}$  underwent significant wetting from 1948 to the 1990s, followed by



**Fig. 1.** Spatial distribution of observed AI climatology during 1991–2020 from 20° to 60°N.



**Fig. 2.** (a) Time series of regional-mean detrended, normalized AI anomaly over the NH from 20° to 60°N during 1948–2021. The red curve is the 11-year moving average. Red (blue) shading denotes decreased (increased) period of the AI. (b) Wavelet spectra of AI anomaly over the NH during 1948–2021. The black line indicates the 95% confidence level. (c) The global power spectrum of AI with the 95% confidence level. (For interpretation of the references to colour in this figure legend, the reader is referred to the web version of this article.)

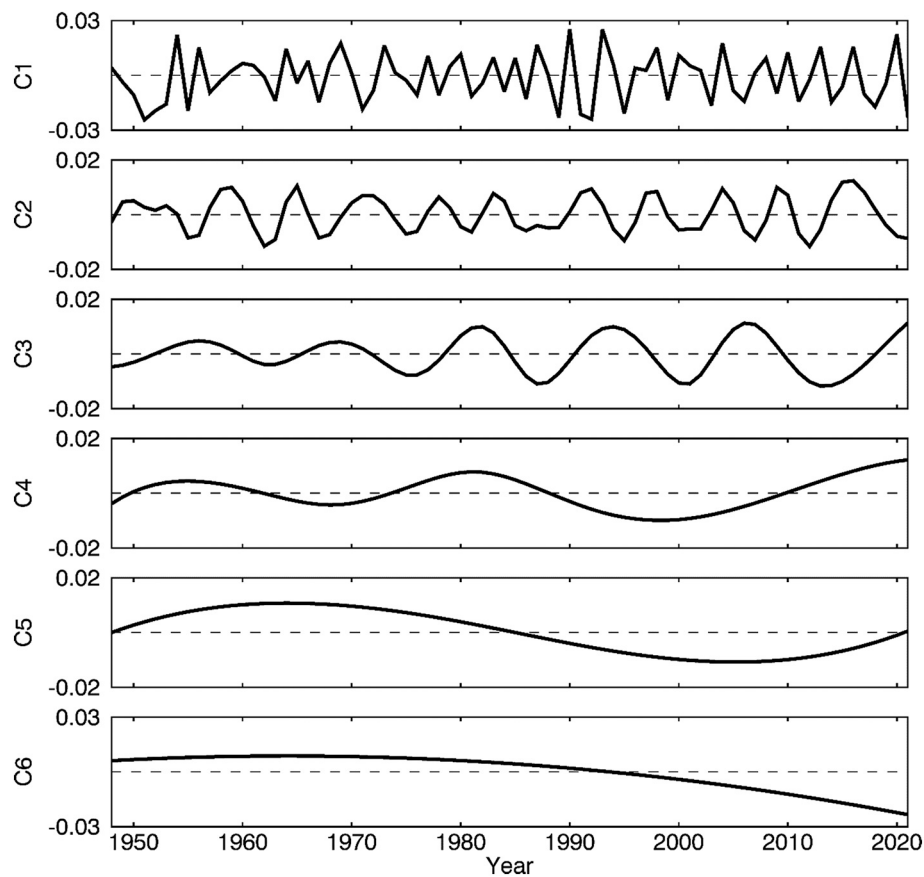


**Fig. 3.** EEMD decomposition of the time series of normalized AI anomaly over the NH land from 20° to 60°N during 1948–2021. C1 to C5 represent five IMFs from high to low frequency, while C6 is the long-term trend.

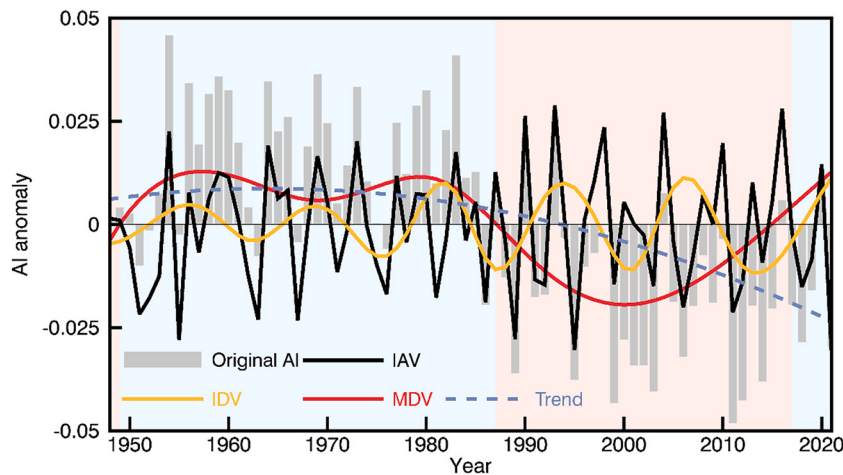


**Fig. 4.** Time series of normalized annual-mean AI anomaly in the NH from 20° to 60°N (grey bar), interannual variation (IAV; black curve), inter-decadal variation (IDV; yellow curve), multi-decadal variation (MDV; red curve), and the long-term trend (blue dashed curve) obtained by EEMD decomposition over the period from 1948 to 2021. Red (blue) shading denotes the negative (positive) period of the MDV. (For interpretation of the references to colour in this figure legend, the reader is referred to the web version of this article.)

subtle drying from the 1990s to 2021. The wetting was obvious in 30° and 40°–60°N from 1948 to 2000. The IAV of the AI changes at a very high frequency and has complicated characteristics at different latitudes (Fig. 5b). The IDV of the AI has different variation in 20°–40°N, 40°–50°N and 50°–60°N. The MDV has distinct dry and wet variation (Fig. 5c); and

its phase changes similarly at different latitudes. It underwent significant wetting in 20°–60°N from 1948 to the 1990s, followed by subtle drying from the 1990s to 2021.

### 3.2. Effects of apparent heat source $Q_1$ over the TP on aridity change in the NH

According to previous results, the MDV is closely associated with ocean oscillation (Guan et al., 2015, 2016, 2019). To explore the multi-decadal effect of the TP on NH aridity, we calculated the effect of  $Q_1$  on the MDV. We regressed the MDV component of the AI over the NH

**Table 1**

Contributions of IAV, IDV, and MDV components to AI.

IAV	IDV	MDV
49%	16%	35%

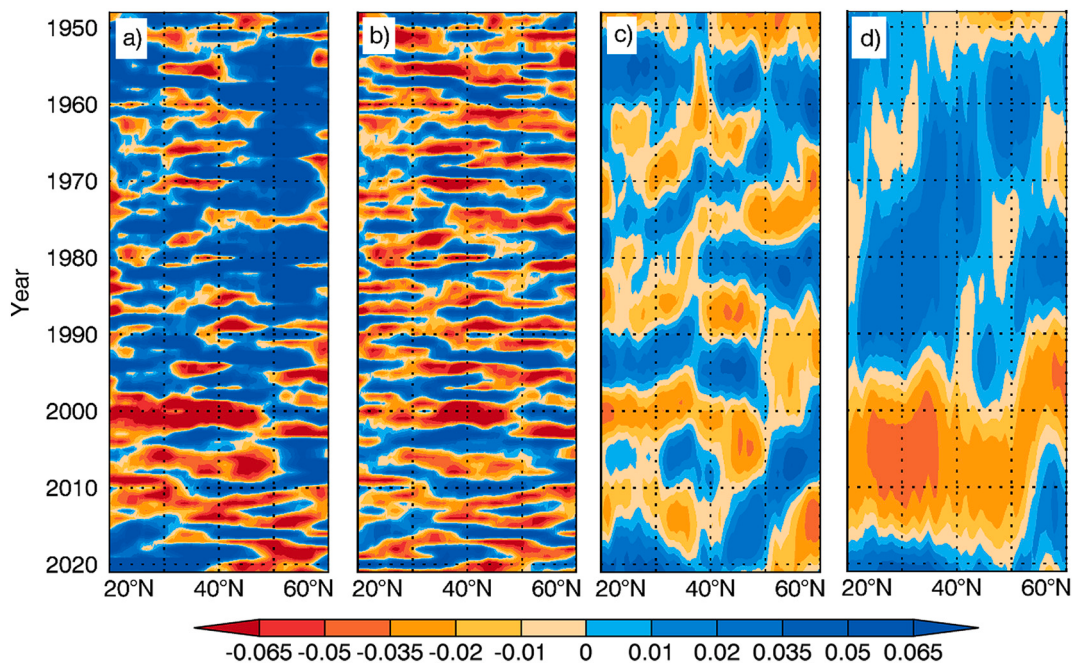


**Fig. 5.** (a) Evolution of zonally averaged annual-mean AI anomalies from 1948 to 2021 over 20°–60°N. (b), (c) and (d) are the same as (a), but for the IAV, IDV and MDV components of the AI, respectively.

**Table 2**  
Contributions of AMO, Q<sub>1</sub>, AO, Nino3.4, and PDO to the regression of the MDV of AI.

AMO	Q <sub>1</sub>	AO	Nino3.4	PDO
62.21%	18.15%	7.85%	7.56%	4.23%

during 1950–2021. The EEMD method was applied to decompose each index (AO, AMO, Nino3.4, PDO, and Q<sub>1</sub>). We obtained six IMFs for each index, and selected the multi-decadal components of each index (IMFs 4 and 5) to regress the MDV component of the AI by using the stepwise multiple linear regression (MLR) method. The regressed MDV can be expressed as follows,

$$AI_{MDV} = -1.45AMO_5 - 34.37AMO_6 - 12.22AO_6 - 1.15Nino_5 - 11.94Nino_6 + 1.16PDO_5 \\ - 8.90PDO_6 + 2.91Q_5 + 18.35Q_6 \quad (9)$$

The regression-based approximation of the MDV component can explain most of its variance using the indices of the AMO, Q<sub>1</sub>, AO,

Nino3.4, and PDO, with contributions of 62.21%, 18.15%, 7.85%, 7.56%, and 4.23%, respectively (Table 2).

### 3.3. Sustained impacts of dynamic and thermal effects of the TP on aridity

Although the Q<sub>1</sub> contribution is much lower than the effects of AMO, the role of the Q<sub>1</sub> on aridity change over the NH cannot be ignored, and the Q<sub>1</sub>-AI relationship is statistically significant. The thermal forcing of the TP has significant influence on the AI. The partial correlation between the MDV of Q<sub>1</sub> and that of the AI is 0.81, which passed the 95% significance test. Fig. 6 shows the spearman's correlation coefficients between the MDV of the AI and that of Q<sub>1</sub> from 1950 to 2021; most of the areas passed the 95% significance test. The AI and Q<sub>1</sub> have positive

---

relationship in Europe, North Africa, central Asia, the Mongolian Plateau, and western Canada; and they have negative relationship in the TP, South Asia and southeastern United States. From 20° to 60°N, 59% of the grid points has the spearman's correlation coefficient above 0.3;

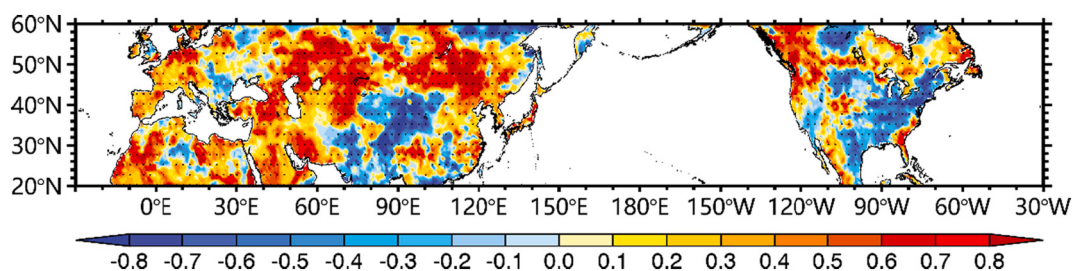


**Fig. 6.** The spearman's correlation coefficient between the MDV of the AI and that of Q<sub>1</sub> from 1950 to 2021. Stippling indicates the 95% confidence level.

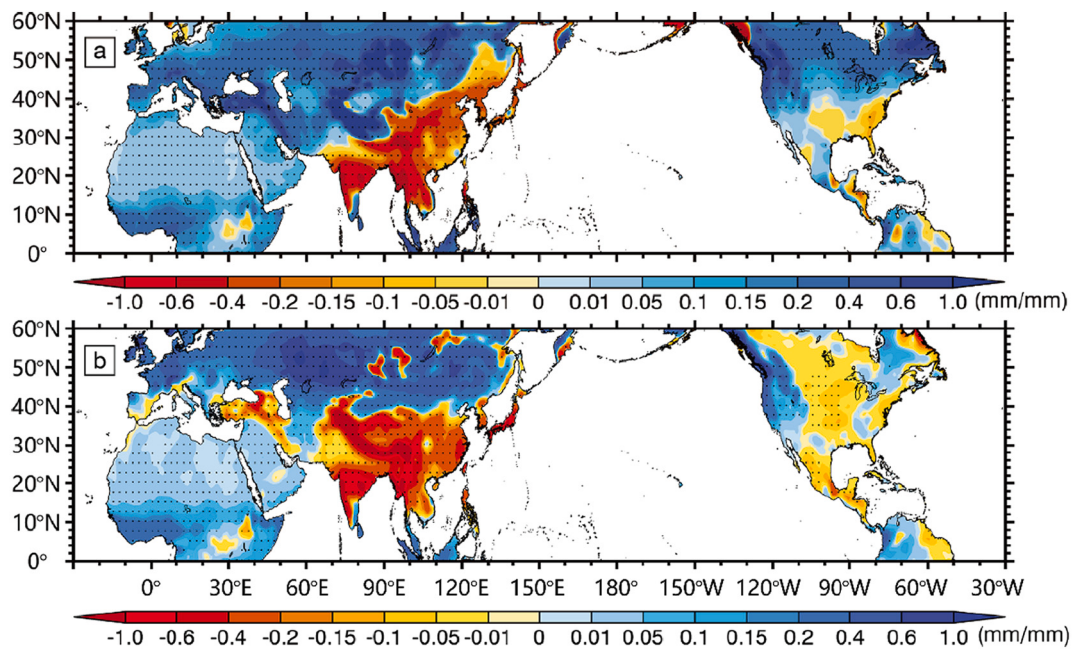


**Fig. 7.** (a) Difference of AI between NTIP-nosh and historical simulations over 1979–2014. The blue area represents the wetting effect of the TP, and vice versa. (b) Difference of AI between NTIP and historical simulations over 1979–2014. The blue area represents the wetting effect of the TP, and vice versa. Stippling indicates the 90% confidence level. (For interpretation of the references to colour in this figure legend, the reader is referred to the web version of this article.)

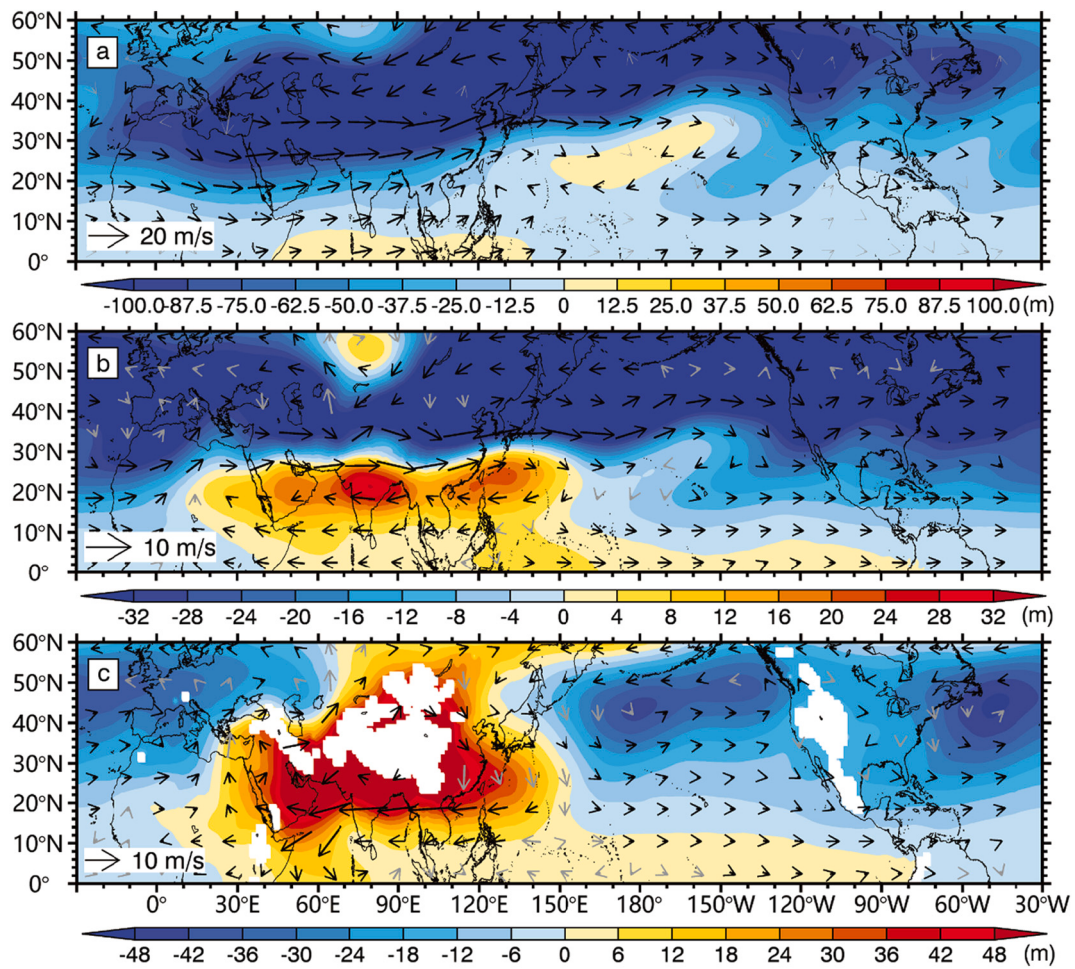


**Fig. 8.** Circulation differences between NTIP-nosh and historical simulations at (a) 200 hPa, (b) 500 hPa and (c) 850 hPa over 1979–2014. Shading represents geopotential height field (units: m), and arrow represents wind field (units: m/s). Black arrow indicates the 90% confidence level.

and 6%, above 0.8. In Asia,  $Q_1$  influences were particularly significant, 66% of the grid points has the spearman's correlation coefficient above 0.3; and 8%, above 0.8.

In addition to the effects of the  $Q_1$  on aridity change in the NH, the uplift of the TP also has sustained impact on the aridity of the NH. The differences of the AI between sensitivity simulation without the TP (NTIP-nosh simulation and NTIP simulation) and that with the TP (historical simulation) over 1979–2014 are shown in Fig. 7. The thermal effect of the TP on the AI; more precisely, the influence of the decrease of TP sensible surface heating to the AI is shown in Fig. 7a. The influence on Asia is obvious.

In Fig. 7a, the drying effect due to the decrease of sensible surface heating of the TP appears over the south and east of the TP; this effect is mainly limited south of 40°N and in Northeast Asia. On the contrary, the wetting effect is over the rest of the NH including North America. Such significant differences between sensitivity experiments without and with the sensible surface heating of the TP (NTIP-nosh and historical simulations) show clear influence of the thermal change of the TP on aridity change. In NTIP, we removed the topography of the TIP at altitude above 500 m. So, Fig. 7b shows the dynamic effect of the TP on the AI, due to the influence of removing the TP. The influence on Asia is obvious.

When the TP topography exists, the influence of TP thermal effect on the AI in Northeast Asia is similar to that south of 40°N in Asia (Fig. 7a). When the TP topography is excluded (Fig. 7b), the influence of the dynamic effect of the TP on the AI shows significant difference in the south and north of 40°N. The latitudinal difference north of 40°N is missing in Fig. 7b, while the meridional difference is obvious in Asia. The

topography of the TP has an impact on North America, with wetting in the west and drying in central North America.

Fig. 8 shows the circulation differences between NTIP-nosh and historical simulations at 200, 500 and 850 hPa. The thermal effect of the TP leads to a positive geopotential height in Asia at 850 hPa; it is significant south of 40°N and extends northward. The negative geopotential height appears over the North Pacific and North Atlantic.

The positive geopotential height extends upward to 500 hPa south of 30°N, centered over India and East of Taiwan Island. The rest of the NH has negative geopotential height, except for 75°E, 50°–60°N, where there is a positive geopotential height. The negative geopotential height covers almost over the entire NH, most significant over Asia, North Pacific and northwestern North America. South Asia, Southeast Asia and South China are controlled by a high-pressure system from 850 to 500 hPa. The negative geopotential height dominates at 200 hPa; the big absolute value region extends from the Baltic coast to Northeast Asia, the North Pacific and northern North America. Positive geopotential height has small absolute value and occurs only in the central Pacific, equatorial Indian Ocean and western equatorial Pacific.

The decrease of sensible surface heating of the TP has a significant influence on the wind field of the NH. An upper-level cyclone is developed over East Asia, which is located in 20°–140°E over 200 hPa and in 80°–140°E over 500 hPa. A low-level anticyclone is developed in 45°–120°E. In the north (south) of the upper-level anticyclone, the easterly (westerly) wind increases because of the sensible surface heating of the TP. In addition, the westerly wind increases significantly at 200 hPa in North Africa and Asia from 15°N to 30°N and in North America from 30°N to 45°N. In the northwest (southeast) of the upper-level

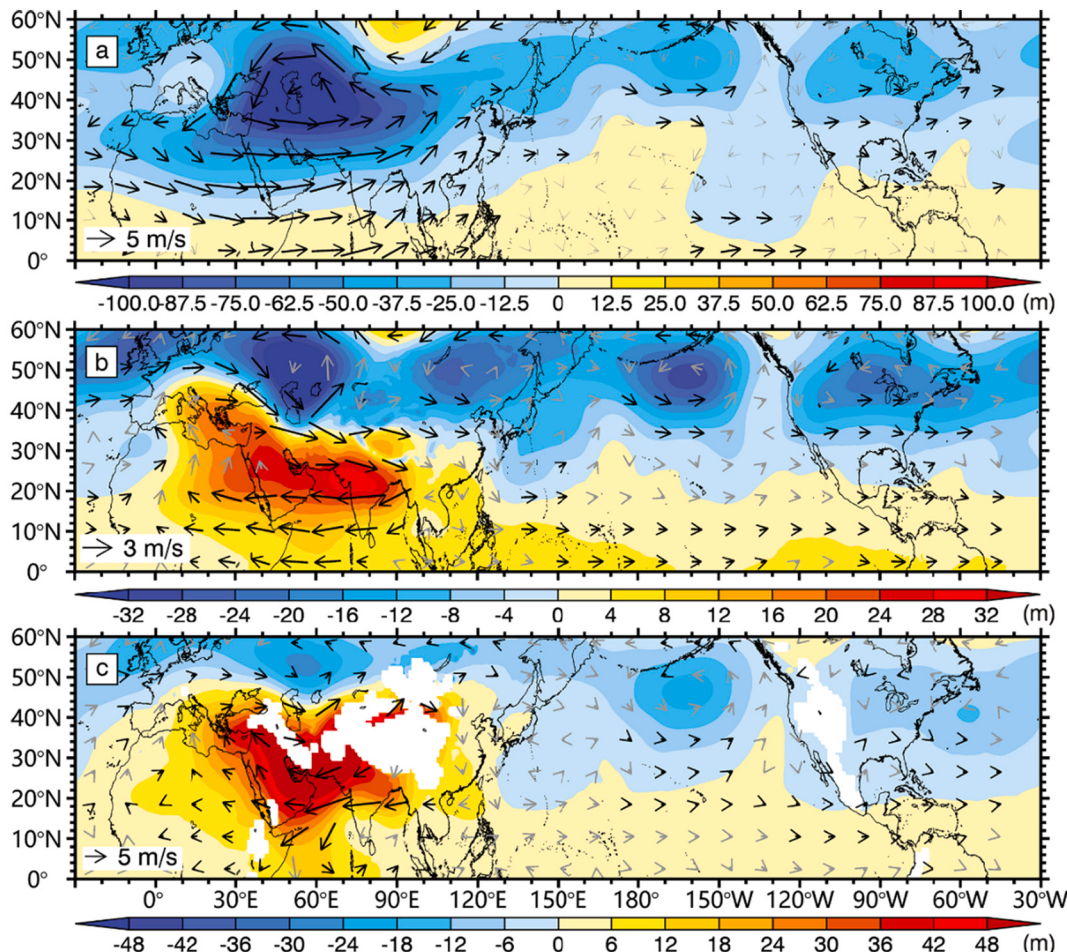
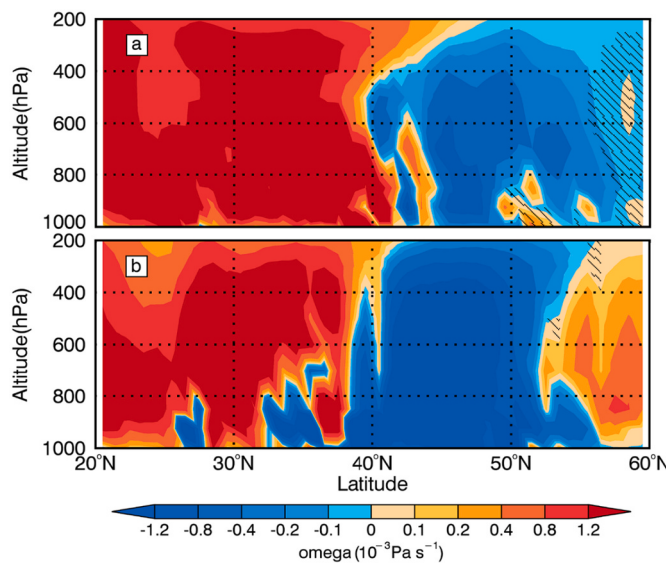


Fig. 9. Same as Fig. 8, except for circulation differences between NTIP and historical simulations.



**Fig. 10.** (a) Differences of zonal-mean omega between NTIP-nosh and historical simulations from 60° to 120°E over 1979–2014. The shading area without hatching indicates the 90% confidence level. (b) Same as (a), but for differences between NTIP and historical simulations.

anticyclone, the northerly (southerly) wind increases because of the decrease of the sensible surface heating of the TP. The southerly wind increases in South Asia, Southeast Asia, and South China. In contrast, the northerly wind increases significantly in the Mongolian Plateau. Thermal changes over the TP lead to more water vapor transported from the western equatorial Pacific and equatorial Indian Ocean to central Asia in the lower atmosphere.

Fig. 9 shows the circulation differences between NTIP and historical simulations at 200, 500 and 850 hPa. Note that Fig. 9 shows overall smaller values than Fig. 8. The dynamic effect of the TP also leads to positive geopotential height in Asia at 850 hPa, but only south of 50°N; there is negative geopotential height north of 50°N. Fig. 9b is similar to Fig. 9c, with positive geopotential height dominated south of 40°N, and negative geopotential height dominated north of 40°N. There are five negative centers north of 40°N, located in 50°E, 110°E, 160°E, 90°W, 10°W, respectively. The negative geopotential height dominates north of 20°N at 200 hPa.

Fig. 10 further illustrate the effect of the thermal changes of the TP on the vertical circulation in Asia. The ascending motion is weakened over 20°–40°N due to the removal of the sensible surface heating of the TP, resulting in drying over 20°–40°N. The ascending motion is strengthened over 40°–55°N due to the removal of the sensible surface heating of the TP, resulting in wetting over 40°–55°N. When the TP topography is excluded (Fig. 10b), the influence of the dynamic effect of the TP on the vertical circulation in Asia exhibits the same characteristics as those in Fig. 10a.

#### 4. Conclusions and discussion

In this study, we found that the MDV is significant in the variability of the AI over the NH. The MDV is closely related to the effects of the ICV in the oceans (AMO, PDO, AO, and ENSO) and over the TP. The TP plays an imperative role in MDV and contributes about 18.15% to the MDV. Meanwhile, the TP has a sustained effect on the AI via the dynamic and thermal effects, especially in Asia. The thermal effect of the TP leads to a drying effect over 20°–40°N in Asia except for the TIP region and Middle East, and a wetting effect in 40°–60°N of the NH except for Northeast Asia. The dynamic effect of the TP leads to meridional differences around 40°N of Asia. The atmospheric circulation field is also influenced by the dynamic and thermal changes associated with the TP. Therefore,

the effect from the TP on the aridity change over 20°–60°N of the NH is a result of both large-scale oscillations and continuous drying/wetting effect.

In the past, the effects of ocean on the decadal to multi-decadal changes of the AI received much attention, with less consideration of the TP. Our results demonstrate the role of the TP on aridity change over the NH cannot be ignored. As the response of the AI to the TP is different over different regions, more work is needed on investigating detailed impact of the TP on regional AI changes and their mechanisms, especially in the boundary regions of the TP.

The interannual variability (IAV) component contributes nearly 50% to AI, and the TP has sustained impacts on aridity in interannual time scale. The IAV component changes at a very high frequency and has complicated characteristics, therefore, it is difficult to quantify the contribution of the TP to AI on interannual time scale by the stepwise multiple linear regression (MLR) method. There is abundant room for further progress in quantifying the contribution of the TP to AI on interannual time scale.

The time series of annual-mean AI anomaly in the NH from 20° to 60°N calculated by our AI data is consistent with that calculated in Feng and Fu (2013) and Huang et al. (2020). The MDV of AI is in a positive phase from 2015 to 2021, so the AI may get wetter in the coming decades over the NH from 20° to 60°N. Sun and Liu (2021) investigated the dynamic and thermal effects of the TP on the precipitation in the Asian arid and monsoon regions, they found that the effect of the TP on the precipitation shows significant difference in the south and north of 40°N. Consistent with Sun and Liu (2021), we found the effect of the TP on the AI also shows significant difference in the south and north of 40°N. Different from Sun and Liu (2021), we focused on the dynamic and thermal effects of the TP on the AI in the NH.

#### CRediT authorship contribution statement

**Zhaokui Gao:** Conceptualization, Methodology, Validation, Writing – original draft, Writing – review & editing, Software, Investigation. **Xiaodan Guan:** Conceptualization, Project administration, Formal analysis, Writing – original draft, Writing – review & editing. **Bian He:** Formal analysis, Data curation. **Long Zhao:** Software, Formal analysis. **Yongkun Xie:** Formal analysis, Writing – review & editing. **Yongli He:** Software. **Fei Ji:** Writing – review & editing.

#### Declaration of Competing Interest

The authors declare that they have no known competing financial interests or personal relationships that could have appeared to influence the work reported in this paper.

#### Data availability

Data will be made available on request.

#### Acknowledgments

This research was funded by the National Natural Science Foundation of China (42041004, 41991231). The authors are grateful to Song Feng ([songfeng@uark.edu](mailto:songfeng@uark.edu)), Guolong Zhang ([zhangguolong@lzu.edu.cn](mailto:zhangguolong@lzu.edu.cn)), Haipeng Yu ([yuhp@lzb.ac.cn](mailto:yuhp@lzb.ac.cn)), and Yun Wei ([weiy16@lzu.edu.cn](mailto:weiy16@lzu.edu.cn)) for supplying the potential evapotranspiration (PET) and aridity index (AI) data sets. Thanks to Jingchen Liu ([liujch18@lzu.edu.cn](mailto:liujch18@lzu.edu.cn)) and Jieru Ma ([majr18@lzu.edu.cn](mailto:majr18@lzu.edu.cn)) for supplying the apparent heat source  $Q_1$  data sets. The oscillation indices are available at <http://climexp.knmi.nl/>. The FGOALS-f3-L outputs, CRU data sets, and PREC/L data are available for download in <https://esgfnode.llnl.gov/projects/cmip6/>, <https://crudata.uea.ac.uk/cru/data/hrg/>, and <https://psl.noaa.gov/data/gridded/data.precl.html>. The data presented in this research are available upon request from the corresponding author.

## References

- Allen, D.G., Pereira, L.O., Raes, D., Smith, M., Allen, R., Pereira, L., Smith, M.A., 1998. *Crop Evapotranspiration: Gigelines for Computing Crop Water Requirements*. Food and Agriculture Organization of the United Nations (FAO), Rome, Italy.
- Chang, C.P., Wang, Z., Ju, J., Li, T., 2004. On the relationship between western maritime continent monsoon rainfall and ENSO during northern winter. *J. Clim.* 17 (3), 665–672. [https://doi.org/10.1175/1520-0442\(2004\)017<0665:OTRBWM>2.0.CO;2](https://doi.org/10.1175/1520-0442(2004)017<0665:OTRBWM>2.0.CO;2).
- Chen, M.Y., Xie, P.P., Janowiak, J.E., Arkin, P.A., 2002. Global land precipitation: a 50-yr monthly analysis based on gauge observations. *J. Hydrometeorol.* 3, 249–266. [https://doi.org/10.1175/1525-7541\(2002\)003%3C0249:GLPAYM%3E2.0.CO;2](https://doi.org/10.1175/1525-7541(2002)003%3C0249:GLPAYM%3E2.0.CO;2).
- Chen, B., Xu, X.D., Yang, S., Bian, J.C., 2012. On the characteristics of water vapor transport from atmosphere boundary layer to stratosphere over Tibetan Plateau regions in summer. *Chin. J. Geophys.* 55, 406–414. <https://doi.org/10.6038/j.issn.0001-5733.2012.02.005>.
- Chen, Z.H., Wen, Q., Yang, H.J., 2021. Impact of Tibetan Plateau on North African precipitation. *Clim. Dyn.* 57, 2767–2777. <https://doi.org/10.1007/s00382-021-05837-2>.
- Enfield, D.B., Mestas-Nunez, A.M., Trimble, P.J., 2001. The Atlantic multidecadal oscillation and its relation to rainfall and river flows in the continental US. *Geophys. Res. Lett.* 28, 2077–2080. <https://doi.org/10.1029/2000GL012745>.
- Feng, S., Fu, Q., 2013. Expansion of global drylands under a warming climate. *Atmos. Chem. Phys.* 13, 10081–10094. <https://doi.org/10.5194/acp-13-10081-2013>.
- Fu, Q., Feng, S., 2014. Responses of terrestrial aridity to global warming. *J. Geophys. Res.-Atmos.* 119. <https://doi.org/10.1002/2014JD021608>.
- Guan, X.D., Huang, J.P., Guo, R.X., Lin, P., 2015. The role of dynamically induced variability in the recent warming trend slowdown over the Northern Hemisphere. *Sci. Rep.* 5. <https://doi.org/10.1038/srep12669>.
- Guan, X.D., Huang, J.P., Zhang, Y.T., Xie, Y.K., Liu, J.J., 2016. The relationship between anthropogenic dust and population over global semi-arid regions. *Atmos. Chem. Phys.* 16, 5159–5169. <https://doi.org/10.5194/acp-16-5159-2016>.
- Guan, X.D., Huang, J.P., Guo, R.X., 2017. Changes in aridity in response to the global warming hiatus. *Journal of Meteorological Research.* 31, 117–125. <https://doi.org/10.1007/s13351-017-6038-1>.
- Guan, X.D., Ma, J.R., Huang, J.P., Huang, R.X., Zhang, L., Ma, Z.G., 2019. Impact of oceans on climate change in drylands. *Science China-Earth Sciences.* 62, 891–908. <https://doi.org/10.1007/s11430-018-9317-8>.
- Harris, I., Jones, P.D., Osborn, T.J., Lister, D.H., 2014. Updated high-resolution grids of monthly climatic observations - the CRU TS3.10 Dataset. *Int. J. Climatol.* 34, 623–642. <https://doi.org/10.1002/joc.3711>.
- He, B., Liu, Y.M., Wu, G.X., Bao, Q., Zhou, T.J., Wu, X.F., Wang, L., Li, J.D., Wang, X.C., Li, J.X., et al., 2020. CAS FGOALS-f3-L model datasets for CMIP6 GMMIP Tier-1 and Tier-3 experiments. *Adv. Atmos. Sci.* 37, 18–28. <https://doi.org/10.1007/s00376-019-9085-y>.
- He, Y.L., Tian, W.L., Huang, J.P., Wang, G., Ren, Y., Yan, H., Yu, H., Guan, X., Hu, H., 2021. The mechanism of increasing summer water vapor over the Tibetan Plateau. *Journal of Geophysical Research: Atmospheres.* 126 <https://doi.org/10.1029/2020JD034166> e2020JD034166.
- Huang, N.E., Shen, Z., Long, S.R., Wu, M.L.C., Shih, H.H., Zheng, Q.N., Yen, N.C., Tung, C.C., Liu, H.H., 1998. The empirical mode decomposition and the Hilbert spectrum for nonlinear and non-stationary time series analysis. *Proceedings of the Royal Society a-Mathematical Physical and Engineering Sciences.* 454, 903–995. <https://doi.org/10.1098/rspa.1998.0193>.
- Huang, J.P., Xie, Y.K., Guan, X.D., Li, D.D., Ji, F., 2017. The dynamics of the warming hiatus over the Northern Hemisphere. *Clim. Dyn.* 48, 429–446. <https://doi.org/10.1007/s00382-016-3085-8>.
- Huang, J.P., Yu, H.P., Han, D.L., Zhang, G.L., Wei, Y., Huang, J.P., An, L.L., Liu, X.Y., Ren, Y., 2020. Declines in global ecological security under climate change. *Ecol. Indic.* 117. <https://doi.org/10.1016/j.ecolind.2020.106651>.
- Jane, Q., 2008. China: the third pole. *Nature.* 454, 393–396. <https://doi.org/10.1038/454393a>.
- Ji, F., Wu, Z.H., Huang, J.P., Chassignet, E.P., 2014. Evolution of land surface air temperature trend. *Nat. Clim. Chang.* 4, 462–466. <https://doi.org/10.1038/nclimate2223>.
- Li, Y.P., Chen, Y.N., Li, Z., 2019. Dry/wet pattern changes in global dryland areas over the past six decades. *Glob. Planet. Chang.* 178, 184–192. <https://doi.org/10.1016/j.gloplacha.2019.04.017>.
- Lickley, M., Solomon, S., 2018. Drivers, timing and some impacts of global aridity change. *Environ. Res. Lett.* 13, 104010 <https://doi.org/10.1088/1748-9326/aae013>.
- Liu, X.D., Dong, B.W., 2013. Influence of the Tibetan Plateau uplift on the Asian monsoon-arid environment evolution. *Chin. Sci. Bull.* 58, 4277–4291. <https://doi.org/10.1007/s11434-013-5987-8>.
- Liu, Y.Z., Li, Y.H., Huang, J.P., Zhu, Q.Z., Wang, S.S., 2020a. Attribution of the Tibetan Plateau to northern drought. *Natl. Sci. Rev.* 7, 489–492. <https://doi.org/10.1093/nsr/nwaa011>.
- Liu, Y.M., Lu, M.M., Yang, H.J., Duan, A.M., He, B., Yang, S., Wu, G.X., 2020b. Land-atmosphere-ocean coupling associated with the Tibetan Plateau and its climate impacts. *Natl. Sci. Rev.* 7, 534–552. <https://doi.org/10.1093/nsr/nwaa011>.
- Liu, J.C., Guan, X.D., Gao, Z.K., Huang, X.Q., Ma, J.R., He, Y.L., Xie, T.J., 2021. Inter-decadal variability of the heat source over the Tibetan Plateau. *Clim. Dyn.* 1–11. <https://doi.org/10.1007/s00382-021-05929-z>.
- Luo, W., Guan, X.D., Xie, Y.K., Liu, J.C., Zhou, Y.B., Zhang, B.D., 2019. The key role of decadal modulated oscillation in recent cold phase. *Int. J. Climatol.* 39, 5761–5770. <https://doi.org/10.1002/joc.6186>.
- Ma, W.Q., Ma, Y.M., 2016. Modeling the influence of land surface flux on the regional climate of the Tibetan Plateau. *Theor. Appl. Climatol.* 125, 45–52. <https://doi.org/10.1007/s00704-015-1495-x>.
- Ma, Y.M., Kang, S.C., Zhu, L.P., Xu, B.Q., Tian, L.D., Yao, T.D., 2008. Tibetan observation and research platform: Atmosphere-land interaction over a heterogeneous landscape. *Bull. Am. Meteorol. Soc.* 89, 1487–1492. <https://doi.org/10.1175/2F1520-0477-89.10.1469>.
- Ma, J.R., Guan, X.D., Guo, R.X., Gan, Z.W., Xie, Y.K., 2017a. Mechanism of non-appearance of hiatus in Tibetan Plateau. *Sci. Rep.* 7, 1–11. <https://doi.org/10.1038/s41598-017-04615-7>.
- Ma, Y.M., Ma, W.Q., Zhong, L., Hu, Z.Y., Li, M.S., Zhu, Z.K., Han, C.B., Wang, B.B., Liu, X., 2017b. Monitoring and Modeling the Tibetan Plateau's climate system and its impact on East Asia. *Sci. Rep.* 7. <https://doi.org/10.1038/srep44574>.
- Mantua, N.J., Hare, S.R., Zhang, Y., Wallace, J.M., Francis, R.C., 1997. A Pacific interdecadal climate oscillation with impacts on salmon production. *Bull. Am. Meteorol. Soc.* 78, 1069–1079. [https://doi.org/10.1175/1520-0477\(1997\)078%3C1069:APICOW%3E2.0.CO;2](https://doi.org/10.1175/1520-0477(1997)078%3C1069:APICOW%3E2.0.CO;2).
- Middleton, N., Thomas, D., 1997. *World Atlas of Desertification*, 3rd ed. Edward Arnold, London, United Kingdom.
- Monteith, J., 1981. Evaporation and surface temperature. *Q. J. R. Meteorol. Soc.* 107, 1–27. <https://doi.org/10.1002/qj.49710745102>.
- Penman, H.L., 1948. Natural evaporation from open water, bare soil and grass. *Proceedings of the Royal Society of London. Series a. Mathematical and Physical Sciences.* 193, 120–145.
- Prlie, R., 2016. Drylands extent and environmental issues. A global approach. *Earth-Science Reviews.* 161, 259–278. <https://doi.org/10.1016/j.earscirev.2016.08.003>.
- Qiao, B.J., Nie, B.K., Liang, C.M., Xiang, L.W., Zhu, L.P., 1984. Spatial Difference of Terrestrial Water Storage Change and Lake Water Storage Change in the Inner Tibetan Plateau. *Remote Sens.* 2021, 13. <https://doi.org/10.3390/rs13101984>.
- Scheff, J., Frierson, D.M.W., 2014. Scaling potential Evapotranspiration with Greenhouse Warming. *J. Clim.* 27, 1539–1558. <https://doi.org/10.1175/JCLI-D-13-00231.1>.
- Sun, H., Liu, X.D., 2021. Impacts of dynamic and thermal forcing by the Tibetan Plateau on the precipitation distribution in the Asian arid and monsoon regions. *Clim. Dyn.* 56, 2339–2358. <https://doi.org/10.1007/s00382-020-05593-9>.
- Thompson, D.W.J., Wallace, J.M., 1998. The Arctic Oscillation signature in the wintertime geopotential height and temperature fields. *Geophys. Res. Lett.* 25, 1297–1300. <https://doi.org/10.1029/98GL00950>.
- Torrence, C., Compo, G.P., 1998. A practical guide to wavelet analysis. *Bull. Am. Meteorol. Soc.* 79, 61–78. [https://doi.org/10.1175/1520-0477\(1998\)079%3C0061:APGTWA%3E2.0.CO;2](https://doi.org/10.1175/1520-0477(1998)079%3C0061:APGTWA%3E2.0.CO;2).
- Trenberth, K.E., 1997. The definition of El Nino. *Bull. Am. Meteorol. Soc.* 78, 2771–2777. [https://doi.org/10.1175/1520-0477\(1997\)078%3C2771:TDOENO%3E2.0.CO;2](https://doi.org/10.1175/1520-0477(1997)078%3C2771:TDOENO%3E2.0.CO;2).
- Trenberth, K.E., Shea, D.J., 2006. Atlantic hurricanes and natural variability in 2005. *Geophys. Res. Lett.* 33. <https://doi.org/10.1029/2006GL026894>.
- Wang, P.X., He, J.H., Zheng, Y.F., Zhang, Q., 2007. Interdecadal relationship between summer Arctic Oscillation and aridity-wetness feature in northwest China. *J. Desert Res.* 27, 883–889.
- Wang, S.S., Huang, J.P., He, Y.L., Guan, Y.P., 2014. Combined effects of the Pacific decadal oscillation and El Nino-southern oscillation on global land dry-wet changes. *Sci. Rep.* 4, 1–8. <https://doi.org/10.1038/srep06651>.
- Wei, Y., Yu, H.P., Huang, J.P., Zhou, T.J., Zhang, M., Ren, Y., 2019. Drylands climate response to transient and stabilized 2 °C and 1.5 °C global warming targets. *Clim. Dyn.* 53, 2375–2389. <https://doi.org/10.1007/s00382-019-04860-8>.
- Wen, Q., Zhu, C.Y., Han, Z.X., Liu, Z.Y., Yang, H.J., 2021. Can the Topography of Tibetan Plateau Affect the Antarctic Bottom Water? *Geophys. Res. Lett.* 48 <https://doi.org/10.1029/2021GL092448> e2021GL092448.
- Wu, Z.H., Huang, N.E., 2009. Ensemble empirical mode decomposition: a noise-assisted data analysis method. *Adv. Adapt. Data Anal.* 1, 1–41. <https://doi.org/10.1142/S1793536909000447>.
- Wu, Y.T., Yang, S., Hu, X.M., Wei, W., 2020. Process-based attribution of long-term surface warming over the Tibetan Plateau. *Int. J. Climatol.* 40, 6410–6422. <https://doi.org/10.1002/joc.6589>.
- Xu, X.D., Lu, C.G., Shi, X.H., Gao, S.T., 2008a. World water tower: An atmospheric perspective. *Geophys. Res. Lett.* 35. <https://doi.org/10.1029/2008GL035867>.
- Xu, X.D., Zhang, R.H., Koike, T., Lu, C.G., Shi, X.H., Zhang, S.G., Bian, L.G., Cheng, X.H., Li, P.Y., Ding, G.A., 2008b. A new integrated observational system over the Tibetan Plateau. *Bull. Am. Meteorol. Soc.* 89, 1492–1496. <https://doi.org/10.1175/2008BAMS2557.1>.
- Xu, X., Zhao, T., Lu, C., Guo, Y., Chen, B., Liu, R., Li, Y., Shi, X., 2014. An important mechanism sustaining the atmospheric "water tower" over the Tibetan Plateau. *Atmos. Chem. Phys.* 14, 11287–11295. <https://doi.org/10.5194/acp-14-11287-2014>.
- Xu, C., Ma, Y.M., Yang, K., You, C., 2018. Tibetan Plateau impacts on global dust transport in the upper troposphere. *J. Clim.* 31, 4745–4756. <https://doi.org/10.1175/JCLI-D-17-0313.1>.
- Yanai, M.H., Tomita, T., 1998. Seasonal and interannual variability of atmospheric heat sources and moisture sinks as determined from NCEP–NCAR reanalysis. *J. Clim.* 11, 463–482. [https://doi.org/10.1175/1520-0442\(1998\)011,0463:SAIVOA.2.0.CO;2](https://doi.org/10.1175/1520-0442(1998)011,0463:SAIVOA.2.0.CO;2).
- Yanai, M.H., Esbensen, S., Chu, J.H., 1973. Determination of bulk properties of tropical cloud clusters from large-scale heat and moisture budgets. *J. Atmos. Sci.* 30, 611–627. [https://doi.org/10.1175/1520-0469\(1973\)030%3c0611:DOBPO%3e2.0.CO;2](https://doi.org/10.1175/1520-0469(1973)030%3c0611:DOBPO%3e2.0.CO;2).
- Yanai, M.H., Li, C.F., Song, Z.S., 1992. Seasonal heating of the Tibetan Plateau and its Effects on the Evolution of the Asian Summer Monsoon. *J. Meteorol. Soc. Jpn.* 70, 319–351. [https://doi.org/10.2151/jmsj1965.70.1B\\_319](https://doi.org/10.2151/jmsj1965.70.1B_319).

- Ye, D.Z., Gao, Y.X., 1979. Meteorology of the Tibetan Plateau. Science press, Beijing, China.
- Ye, D.Z., Wu, G.X., 1998. The role of the heat source of the Tibetan Plateau in the general circulation. *Meteorog. Atmos. Phys.* 67, 181–198. <https://doi.org/10.1007/BF01277509>.
- You, Q.L., Chen, D.L., Wu, F.Y., Pepin, N., Cai, Z.Y., Ahrens, B., Jiang, Z.H., Wu, Z.W., Kang, S.C., AghaKouchak, A., 2020. Elevation dependent warming over the Tibetan Plateau: patterns, mechanisms and perspectives. *Earth Sci. Rev.* 210, 103349. <https://doi.org/10.1016/j.earscirev.2020.103349>.
- Zhang, L.X., Zhou, T.J., 2015. Drought over East Asia: a Review. *J. Clim.* 28, 3375–3399. <https://doi.org/10.1175/JCLI-D-14-00259.1>.
- Zhang, Y.C., Kuang, X.Y., Guo, W.D., Zhou, T.J., 2006. Seasonal evolution of the upper-tropospheric westerly jet core over East Asia. *Geophys. Res. Lett.* 33, 317–324. <https://doi.org/10.1029/2006GL026377>.
- Zhou, T.J., Chen, X.L., He, B., Wu, B., Zhang, L.X., 2019. Short commentary on CMIP6 Global Monsoons Model Intercomparison Project (GMMIP). *Adv. Clim. Chang. Res.* 15, 493. <https://doi.org/10.12006/j.issn.1673-1719.2019.132>.